The Large-Scale, Long-Term Coupling of Temperature, Hydrology, and Water Isotopes®

Nicholas Siler, ^a Adriana Bailey, ^b Gerard H. Roe, ^c Christo Buizert, ^a Bradley Markle, ^d and David Noone ^e

^a College of Earth, Ocean, and Atmospheric Sciences, Oregon State University, Corvallis, Oregon
 ^b National Center for Atmospheric Research, Boulder, Colorado
 ^c Department of Earth and Space Sciences, University of Washington, Seattle, Washington
 ^d Department of Geological Sciences, University of Colorado, Boulder, Colorado
 ^e Department of Physics, University of Auckland, Auckland, New Zealand

(Manuscript received 16 July 2020, in final form 21 April 2021)

ABSTRACT: The stable isotope ratios of oxygen and hydrogen in polar ice cores are known to record environmental change, and they have been widely used as a paleothermometer. Although it is known to be a simplification, the relationship is often explained by invoking a single condensation pathway with progressive distillation to the temperature at the location of the ice core. In reality, the physical factors are complicated, and recent studies have identified robust aspects of the hydrologic cycle's response to climate change that could influence the isotope–temperature relationship. In this study, we introduce a new zonal-mean isotope model derived from radiative transfer theory and incorporate it into a recently developed moist energy balance climate model (MEBM), thus providing an internally consistent representation of the physical coupling between temperature, hydrology, and isotope ratios in the zonal-mean climate. The isotope model reproduces the observed pattern of meteoric δ^{18} O in the modern climate and allows us to evaluate the relative importance of different processes for the temporal correlation between δ^{18} O and temperature at high latitudes. We find that the positive temporal correlation in polar ice cores is predominantly a result of suppressed high-latitude evaporation with cooling, rather than local temperature changes. The same mechanism also explains the difference in the strength of the isotope–temperature relationship between Greenland and Antarctica.

KEYWORDS: Energy transport; Hydrologic cycle; Climate change; Energy budget/balance; Paleoclimate

1. Introduction

The proportions of different isotopes in atmospheric water reflect the full set of hydrologic processes that add, remove, transport, and mix the gaseous, liquid, and solid constituents of that water. Because many of these processes are temperature dependent, the isotopic composition of water that precipitates to the surface reflects the combined hydrologic and temperature history of the vapor from which it condenses. Geologic repositories of precipitation isotope ratios, such as speleothems and polar ice cores, thus provide a crucial source of information about past hydroclimate states.

The physical controls on isotopic fractionation have long been studied as a branch of chemistry (e.g., Urey 1947), and that understanding has been used to infer the environmental conditions reflected in the isotope ratios of atmospheric water, and especially precipitation (e.g., Dansgaard 1964). Because water vapor is often transported thousands of kilometers along complex trajectories (Trenberth 1998), precipitation that falls at any one location reflects the aggregated histories of vapor parcels that have evaporated from vastly different regions (Johnsen et al. 1989; Sodemann and Stohl 2009; Singh et al.

© Supplemental information related to this paper is available at the Journals Online website: https://doi.org/10.1175/JCLI-D-20-0563.s1.

Corresponding author: Nicholas Siler, nick.siler@oregonstate.edu

2016a). For this reason, the isotope ratios in precipitation are an inherently integrative measure of the global hydroclimate. This is both a strength and a weakness. It is a strength because the isotopic composition of precipitation at a single location can be assumed to reflect large-scale information about the atmospheric state. But it is also a weakness because the full set of processes that the water vapor experienced on all of the trajectories that ultimately led to precipitation at one location greatly complicates the interpretation of those records.

Given this physical complexity, it is perhaps surprising that robust statistical relationships are widely observed between precipitation isotope ratios and local climate variables (e.g., Galewsky et al. 2016). Most notably, in the middle and high latitudes, the δ^{18} O and δ^{2} H of precipitation are strongly correlated with local surface temperature (e.g., Dansgaard 1964; Jouzel et al. 1997). This "temperature effect" is often interpreted as a result of Rayleigh distillation, operating within a simple model of the extratropical hydrologic cycle that consists of a continuous stream of water vapor that evaporates from the subtropical oceans and progressively condenses as it moves poleward to cooler temperatures. Assuming constant Rayleigh fractionation and a source temperature of 20°C, Dansgaard (1964) showed that this model implies a spatial regression slope between precipitation δ^{18} O (δ_p) and surface temperature of around 0.7% K⁻¹, which closely matches the relationship found in observations. If one further assumes that the source temperature is relatively constant in time, the same result can also be applied to the temporal regression slope, allowing historical temperatures to be reconstructed from δ_n variations

recorded in polar ice cores (Grootes et al. 1993; Jouzel et al. 1997; Johnsen et al. 2001; Jouzel et al. 2003; Masson-Delmotte et al. 2006). However, independent temperature reconstructions from boreholes (Johnsen et al. 1995; Cuffey et al. 1994, 1995; Dahl-Jensen et al. 1998) and nitrogen isotopes (Severinghaus et al. 1998; Buizert et al. 2014; Kindler et al. 2014) suggest that the temporal regression slope between temperature and δ_p at a given site can differ substantially from the observed spatial slope, with values ranging from less than 0.4% K⁻¹ in Greenland to more than 1% K⁻¹ in Antarctica (e.g., Buizert et al. 2021). This difference between spatial and temporal slopes should not be surprising given that δ_p is known to be sensitive to multiple environmental factors besides local temperature, such as changes in the seasonality of precipitation (Krinner et al. 1997; Werner et al. 2000), shifting atmospheric circulation patterns (Charles et al. 1994; Rhines and Huybers 2014), and changes in the temperature and spatial distribution of evaporation source regions (Boyle 1997; Masson-Delmotte 2005; Werner et al. 2001; Sodemann et al. 2008; Lee et al. 2008). Indeed, given this complexity, the bigger surprise may be that δ_p is correlated with local temperature at all. Such correlations seem to indicate an underlying coherence to the hydroclimate system, whereby a change in one variable necessarily implies synchronous changes in all the others.

In recent years, research into anthropogenic warming has led to substantial progress in understanding the hydrologic cycle and its role in the global climate system. In the global mean, the latent heat of evaporation and condensation must be balanced by other terms in the energy budgets of the surface and atmosphere (Boer 1993; Allen and Ingram 2002). This, combined with thermodynamic constraints on the partitioning between latent and sensible heat fluxes from the surface (e.g., Siler et al. 2019), acts as a strong constraint on evaporation (and hence precipitation, since water must be conserved). As a result, GCM simulations tend to show a relatively modest increase in global-mean precipitation of 2%-3% K⁻¹ of globalmean warming—substantially less than the \sim 7% K^{-1} increase in atmospheric water vapor expected from the Clausius-Clapeyron equation (e.g., Allen and Ingram 2002; Held and Soden 2006). If the basic structure and intensity of the atmospheric circulation remains similar, the mean-state patterns of moisture transport and convergence will increase with warming at a similar rate as water vapor, implying wetter deep tropics, drier subtropics, and wetter middle and high latitudes (Held and Soden 2006). Furthermore, because vapor and vapor transport increase at a larger rate globally than precipitation or evaporation, simple scaling arguments imply that water vapor will also travel farther and reside longer in the atmosphere, on average, as the climate warms (Trenberth 1998; Singh et al. 2016b).

Recent studies have further demonstrated that the spatial patterns of temperature and hydrologic change are tightly coupled through their joint dependency on meridional atmospheric heat transport, of which latent heat (and hence hydrology) is a key component. In particular, Siler et al. (2018) showed that the spatial patterns of zonal-mean temperature and hydrology in the current climate—as well as the spatial patterns of temperature and hydrologic change predicted

within an ensemble of GCMs—can be accurately emulated using a simple one-dimensional (1D) energy balance model, in which poleward energy transport is represented as the linear diffusion of near-surface moist static energy (i.e., sensible plus latent heat).

This energetic framework provides a self-consistent understanding of the coupling between zonal-mean hydrology and surface temperature, both in the modern climate and in the context of climate changes. In this paper, we add to this framework a simple representation of Lagrangian vapor transport and Rayleigh fractionation. We show that the fractionation of isotopes due to evaporation, meridional transport, and precipitation can be represented mathematically by the equations of radiative transfer. Using this framework, we can reproduce the observed meridional distribution of δ_p in the modern climate, suggesting the observed patterns are the result of a few simple principles.

We also investigate the cause of the observed positive temporal regression slope between δ_p and temperature at high latitudes. We find that predicted changes in temperature and vapor transport distance would, by themselves, cause the temporal slope to be negative. We conclude that the positive slope found in the ice core record primarily reflects the sensitive dependence of evaporation on the mean-state climate, and hence a redistribution of evaporation patterns with climate change, which is a predictable consequence of thermodynamic constraints on the partitioning of surface energy fluxes.

2. Meridional vapor transport: A 1D Lagrangian perspective

Any representation of Rayleigh fractionation requires a method of tracking, in a Lagrangian sense, the movement of water vapor from its source (where it evaporates) to its sink (where it precipitates). Here we present a simple Lagrangian model of meridional vapor transport, which derives from the essential similarity between the depletion of vapor transport by precipitation and the attenuation of radiation through scattering or absorption.

In radiative transfer, when a beam of light propagates through a scattering or absorbing medium, the intensity I of the beam progressively decreases. The fractional decrease in I per distance of propagation is defined as the attenuation coefficient μ :

$$\mu(x) \equiv -\frac{1}{I}\frac{dI}{dx}.\tag{1}$$

As the beam propagates between two points, x_1 and x_2 , it experiences a cumulative attenuation of

$$\tau(x_1, x_2) = \int_{x_1}^{x_2} \mu(x) \, dx,\tag{2}$$

which is defined as the optical depth of the layer. The decrease in intensity across the layer is given by Beer's law,

$$\frac{I(x_2)}{I(x_1)} = f(x_1, x_2), \tag{3}$$

where

$$f(x_1, x_2) = e^{-\tau(x_1, x_2)} \tag{4}$$

represents the transmittance of the layer.

We can apply these same equations to the zonal-mean hydrologic cycle, where the depletion of vapor transport by precipitation is similar to the attenuation of light by absorption and scattering. In this analogy, the attenuation coefficient [Eq. (1)] represents the fraction of vapor that condenses per distance x of meridional transport. In the time average, this is given by

$$\mu(x) \approx 2\pi a^2 \frac{P(x)}{|F(x)|},\tag{5}$$

where x is the sine of latitude, a is Earth's radius, P is the zonal-mean precipitation rate at the surface (in units of latent heat flux, W m⁻²), and F is the zonally integrated net northward latent heat transport (in W). Because F must vanish at the poles, and the meridional divergence of F is proportional to the zonal-mean evaporation E minus P, we can write

$$F(x) = 2\pi a^2 \int_{-1}^{x} E(\tilde{x}) - P(\tilde{x}) d\tilde{x}.$$
 (6)

Thus, $\mu(x)$ depends only on the zonal-mean patterns of E and P. We can then use Eqs. (2) and (4) to define hydrologic analogs to $\tau(x_1, x_2)$ and $f(x_1, x_2)$, with the latter representing the fraction of vapor that evaporates at a particular source latitude x_1 and reaches a downstream latitude x_2 without precipitating. To be physically realistic, we set $f(x_1, x_2) = 0$ for all x_2 that are not directly downstream from x_1 , as determined by the sign of E.

The above framework allows us to characterize meridional vapor transport from both a source and sink perspective. First, from the source perspective, we define $w_e(x_1, x_2)$ as the distribution of precipitation across all x_2 that results from evaporation at a single source latitude x_1 . Expressed as a probability density function (PDF), this distribution is equal to the absolute value of $\partial f/\partial x_2$, which simplifies to

$$w_{e}(x_{1}, x_{2}) = \mu(x_{2})f(x_{1}, x_{2}).$$
 (7)

Second, from the sink perspective, we define $w_p(x_1, x_2)$ as the meridional distribution of evaporation that results in precipitation at a particular sink latitude. As noted by Fisher (1990), this is proportional to $f(x_1, x_2)$, weighted by the magnitude of evaporation at the source:

$$w_p(x_1, x_2) = \frac{f(x_1, x_2)E(x_1)}{\int_{-1}^1 f(x_1, x_2)E(x_1) dx_1}.$$
 (8)

The difference between these two perspectives is illustrated in the second row of Fig. 1, which shows examples of w_e (Fig. 1c) and w_p (Fig. 1d) at representative source and sink latitudes of $\sin^{-1}x_1 = \pm 40^\circ$ and $\sin^{-1}x_2 = \pm 80^\circ$, respectively, computed using annual-mean values of E(x) and P(x) from ERA5 reanalysis (Figs. 1a,b; Hersbach et al. 2020). The w_e PDFs (Fig. 1c) are almost mirror images of each other, decaying

roughly exponentially from each source latitude toward its respective pole. By comparison, the PDFs of w_p (Fig. 1d) exhibit more spatial structure and less symmetry, with a narrower distribution and sharper local peak in the Northern Hemisphere (red) than in the Southern Hemisphere (blue). This asymmetry is not caused by differences in the spatial pattern of $f(x_1, x_2)$, which is similar between the hemispheres. Rather, it stems from E(x), which is greater at high latitudes in the Northern Hemisphere than in the Southern Hemisphere (Fig. 1a, red line), thereby giving more weight to northern high-latitude sources in Eq. (8).

From the PDFs of w_e and w_p , we can also calculate the average distance that vapor travels from and to a given latitude. The meridional distance traveled by a single vapor molecule over its lifetime is equal to $a|\theta_2 - \theta_1|$, where $\theta_1 = \sin^{-1}x_1$ and $\theta_2 = \sin^{-1}x_2$ are the source and sink latitudes, respectively (in radians). Therefore, the average meridional transport distance of *all* vapor originating at x_1 , defined here as $\overline{d_e}(x_1)$, is equal to the average of $a|\theta_2 - \theta_1|$ over all sink latitudes, weighted by w_e :

$$\overline{d_e}(x_1) = \int_{-1}^1 a|\theta_2 - \theta_1| w_e(x_1, x_2) dx_2. \tag{9}$$

Because the attenuation coefficient μ tends to exhibit little variability over small spatial scales, we show in appendix A that Eq. (9) can be approximated as

$$\overline{d_e}(x_1) \approx \frac{a}{\cos \theta_1} \mu(x_1)^{-1}. \tag{10}$$

Therefore, just as in radiative transfer (e.g., Wallace and Hobbs 2006), μ can be interpreted as an inverse length scale of vapor transport, with large values implying that vapor travels a short distance before precipitating. Conversely, from a sink perspective, vapor that *precipitates* at a particular latitude will have traveled an average distance of

$$\overline{d_p}(x_2) = \int_{-1}^1 a|\theta_2 - \theta_1| w_p(x_1, x_2) dx_1. \tag{11}$$

Equations (9) and (11) represent two distinct ways of defining the average vapor transport distance. Whereas $\overline{d_e}$ measures how far vapor travels from a particular source latitude, $\overline{d_p}$ measures how far vapor travels to a particular sink latitude. The results of these contrasting perspectives are shown in the bottom row of Fig. 1, along with the approximate form of $\overline{d_e}$ given by Eq. (10) (Fig. 1e, dashed lines). These were computed using annual-mean values of E(x) and P(x), so they underestimate the true transport distance in much of the tropics, where the direction of F changes with the seasons. Poleward of $\sim 20^{\circ}$, however, the impact of seasonal variability is small (see supplemental Fig. 1 in the online supplemental material). At these latitudes, the two definitions of transport distance diverge sharply. From the source perspective (Fig. 1e), $\overline{d_e}$ is approximately symmetric between the Northern and Southern Hemispheres, reaching a maximum of around 1000 km near 40° and decreasing roughly linearly to zero at the poles. This behavior is captured well by the approximation in Eq. (10) (dashed line), demonstrating that d_e mostly reflects an increase in μ with latitude. From the sink perspective, however, transport distance $\overline{d_p}$ generally increases with latitude outside the

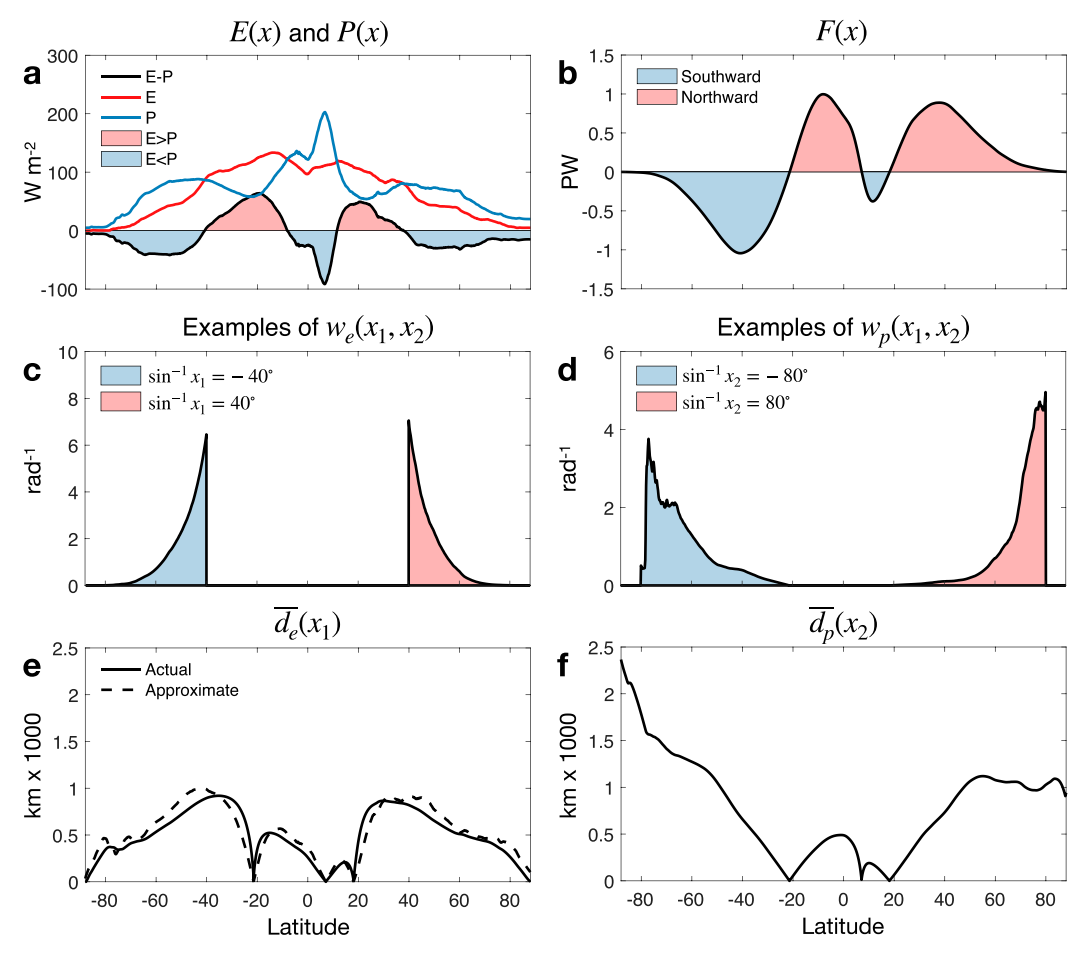


FIG. 1. (a) Zonal-mean, annual-mean E (red), P (blue), and E - P (black) in the modern climate (1979–2018), from ERA5 reanalysis. Red (blue) shading indicates latitudes where E > P (E < P). (b) Zonal-mean, annual-mean net northward atmospheric latent heat flux. Blue (red) shading indicates net southward (northward) transport. (c) $w_e(x_1, x_2)$ at representative source latitudes of -40° (blue) and 40° (red), representing the spatial distribution of precipitation that results from evaporation at these latitudes (to convert from units of x^{-1} to θ^{-1} , we multiply by $dx/d\theta = \cos\theta$). (d) $w_p(x_1, x_2)$ at representative sink latitudes of -80° (blue) and 80° (red), representing the spatial distribution of evaporation that contributes to precipitation at these latitudes (in units of θ^{-1}). (e) The average distance vapor travels from each source latitude, from Eq. (9) (solid line) and Eq. (10) (dashed line). (f) The average distance vapor travels to each sink latitude from Eq. (11).

tropics (Fig. 1f), implying that precipitation at high latitudes originates from farther away than precipitation at lower latitudes. The spatial pattern of $\overline{d_p}$ is also highly asymmetric at high latitudes, with much larger values in the Southern Hemisphere than in the Northern Hemisphere. Like the hemispheric differences in w_p discussed previously (Fig. 1d), this asymmetry in $\overline{d_p}$ stems from asymmetry in E, which causes a larger fraction of high-latitude precipitation in the Southern Hemisphere to originate from remote sources. This asymmetry will prove to be crucial to understanding the hemispheric differences in δ_p at high latitudes.

3. Isotope model

Just as $\overline{d_p}$ represents the weighted-average transport distance of all upstream sources [Eq. (11)], the average value of δ_p at a particular latitude is given by

$$\overline{\delta_p}(x_2) = \int_{-1}^1 \delta_p(x_1, x_2) w_p(x_1, x_2) dx_1, \tag{12}$$

where $\delta_p(x_1, x_2)$ is the δ of precipitation at x_2 that results from evaporation at x_1 . By definition, this is related to the isotope ratio R_p by

$$\delta_p(x_1, x_2) = \left[\frac{R_p(x_1, x_2)}{R_{\text{std}}} - 1\right] \times 1000,$$
 (13)

where R_{std} is the isotope ratio of Vienna Standard Mean Ocean Water (VSMOW), and the factor of 1000 reflects the conversion to permil $\binom{9}{90}$.

To find $\overline{\delta_p}(x_2)$, let us first consider a single vapor parcel that evaporates at x_1 with an initial isotope ratio of $R_e(x_1)$, and then progressively condenses as it is transported to the north or

south. Along the way, the isotope ratio of the vapor (R_v) evolves according to

$$\frac{D\ln R_{v}}{Dx} = (\alpha - 1)\frac{D\ln q}{Dx},\tag{14}$$

where α is the effective fractionation factor and $D\ln q/Dx$ is the fractional change in the parcel's specific humidity with latitude, which is equal and opposite to the fractional condensation rate (note that D/Dx represents the material derivative following the parcel). Equilibrium values of α vary from 1.009 at 30°C to 1.025 at -50° C (Majoube 1970, 1971), but at temperatures below -20° C the increase with cooling is mostly offset by nonequilibrium kinetic effects (see appendix B and supplemental Fig. 2). We account for these dependencies later, but for now let us assume that α is constant, and equal to the global average effective fractionation. This allows us to integrate Eq. (14) directly, yielding

$$R_{\nu}(x_1, x_2) \approx R_{\nu}(x_1) f(x_1, x_2)^{\alpha - 1},$$
 (15)

where $f(x_1, x_2)$ is the hydrologic transmittance [Eq. (4)]. Equation (15) is equivalent to Rayleigh distillation along a meridional pathway. Assuming that the isotopic content of condensed water is conserved as it falls to the surface, the isotope ratio of precipitation is then given by

$$R_{n}(x_{1}, x_{2}) = \alpha R_{n}(x_{1}, x_{2}). \tag{16}$$

Now suppose that evaporation and condensation exhibit roughly the same fractionation, such that $\alpha \approx R_{\rm std}/R_e$. Applying the first-order Taylor approximation, $f^{\alpha-1} \approx 1 + (\alpha+1)\ln(f)$, Eqs. (12)–(16) combine to give

$$\overline{\delta_p}(x_2) \approx -\varepsilon \overline{\tau}(x_2),$$
 (17)

where ε is defined in the conventional way,

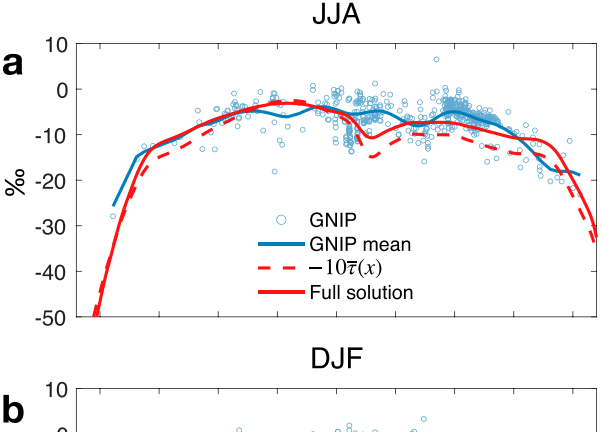
$$\varepsilon \equiv (\alpha - 1) \times 1000, \tag{18}$$

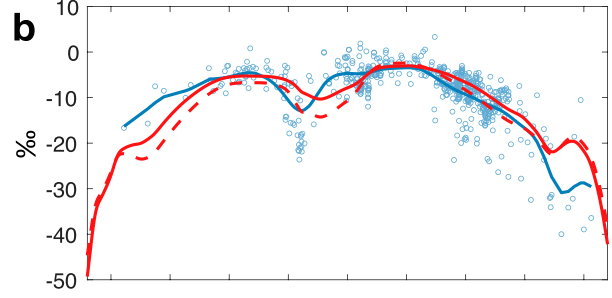
and

$$\overline{\tau}(x_2) = \int_{-1}^{1} \tau(x_1, x_2) w_p(x_1, x_2) dx_1.$$
 (19)

Thus, the average value of δ_p at a given latitude scales approximately linearly with $\overline{\tau}$, which represents the average path-integrated attenuation experienced by all vapor present at that latitude.

To test how well Eq. (17) captures the distribution of $\overline{\delta_p}$ of 18 O in the modern climate, we compute $\overline{\tau}(x_2)$ using observed zonal-mean values of E(x) and P(x) from ERA5 reanalysis, and set $\varepsilon=10\%$ everywhere, following Bailey et al. (2018). Figures 2a–c show the resulting meridional profiles of $\overline{\delta_p}$ (dashed red line) during boreal summer (July–August), boreal winter (December–February), and the annual mean, computed using average profiles of E and P from each time period. Blue circles represent observed values of δ_p from rain gauges and—in the annual mean—Antarctic snow. At all latitudes and across the annual cycle, the predicted values of $\overline{\delta_p}$ capture much of the





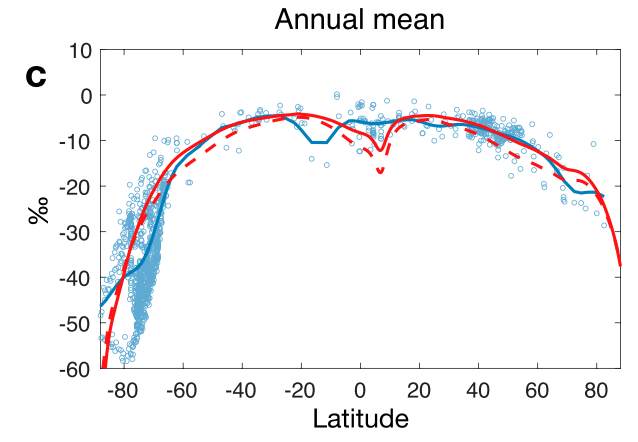


FIG. 2. Average δ^{18} O of precipitation in (a) June–August and (b) December–February, and (c) the annual mean. Blue dots indicate observations from the International Atomic Energy Agency/Global Network of Isotopes in Precipitation (GNIP) dataset. Seasonal data come from rain gauges, while annual data come from rain gauges and Antarctic snow. Blue lines show the zonal mean of observations, computed using a moving Gaussian filter with $\sigma=4^\circ$ latitude. The dashed red line shows the approximation of $\overline{\delta_p}$ assuming constant fractionation of 10% [Eq. (17)], computed using seasonal or annual means of E(x) and P(x) from ERA5. The solid line shows the full solution for $\overline{\delta_p}$ that accounts for the influence of temperature and kinetic effects on fractionation.

observed meridional pattern (blue line). In the tropics, seasonal variations in $\overline{\delta_p}$ coincide with the migration of the intertropical convergence zone into the summer hemisphere, indicating a negative correlation with precipitation that is consistent with the "amount effect" (Dansgaard 1964). The model also captures most of the hemispheric asymmetry in $\overline{\delta_p}$ in the annual mean (Fig. 2c), correctly predicting more negative

values at high latitudes in the Southern Hemisphere than in the Northern Hemisphere. Because $\tau(x_1, x_2)$ generally increases with transport distance $(\theta_2 - \theta_1)$, this asymmetry is closely tied to the hemispheric differences in $\overline{d_p}$ discussed in section 2.

Our approximation of $\overline{\delta_p}$ can be made somewhat more realistic by accounting for spatial variability in α and R_e . To do this, we approximate α as a function of surface temperature T_s using the empirical equations of Majoube (1970, 1971), and adjust for kinetic effects at subfreezing temperatures (see appendix B). For $R_e(x)$, we use the Craig–Gordon model (Craig and Gordon 1965), which takes into account nonequilibrium kinetic effects, as well as the temperature and isotope ratio of the near-surface atmosphere (see appendix C).

The solid red lines in Figs. 2a–c show the resulting profiles of $\overline{\delta_p}$ when these approximations for α and R_e are incorporated in Eq. (12). Compared with the simpler approximation in Eq. (17) (dashed red line), the full solution exhibits less depletion of ¹⁸O at low latitudes, reflecting less fractionation during evaporation when using the more sophisticated Craig-Gordon model (supplemental Fig. 3). At high latitudes, this difference is mostly offset by greater fractionation during condensation at cold temperatures (Majoube 1970, 1971; see supplemental Fig. 2), resulting in better agreement between the two $\overline{\delta_p}$ profiles.

While the full solution agrees somewhat better with observations at most latitudes, the two solutions are quite similar overall, supporting the conclusion of Bailey et al. (2018) that most of the observed spatial and temporal variability in $\overline{\delta_p}$ can be explained by the spatial patterns of E and P. In the next section, we apply this result to better understand the response of $\overline{\delta_p}$ to climate change.

4. The isotopic response to Last Glacial Maximum climate change

The preceding analysis shows that the spatial pattern of the climatology of $\overline{\delta_p}$ depends on E(x), P(x), and $T_s(x)$. We therefore anticipate that the sensitivity of $\overline{\delta_p}$ to climate change will depend on the full spatial structure of temperature and hydrologic change, and not just on local temperature.

We now consider three idealized scenarios to isolate the impact of different aspects of hydroclimate change. The first scenario is a spatially uniform temperature change and a uniform evaporation sensitivity that scales at the global-mean rate, reflecting the well-known approximations of Held and Soden (2006); the second scenario includes the impact of polar amplification of temperature change, as represented by a moist-static energy balance model (Roe et al. 2015; Siler et al. 2018); and the third scenario includes the strong temperature dependence of evaporation sensitivity, which is derived from the Penman surface energy balance equation (Siler et al. 2019).

Our main interest is what controls the temporal regression slope between $\overline{\delta_p}$ (in ¹⁸O) and T_s at high latitudes, since variability in δ_p in ice cores is widely used for paleothermometry. For each scenario, we compute the temporal slope at each latitude based on the change in $\overline{\delta_p}$ that results from a global-mean cooling representative of the Last Glacial Maximum (LGM), and compare our result with independent estimates of the temporal slope based on analyses of ice cores from

Greenland and Antarctica. Throughout this analysis, we will use the notation []' to indicate the change in a variable relative to its modern-day value.

a. Scenario 1: Uniform temperature change and uniform evaporation sensitivity

The analyses for the first scenario are presented in Fig. 3. We impose a spatially uniform cooling of $T_s' = -5 \,\mathrm{K}$ (Fig. 3a), which roughly approximates the global-mean temperature of the LGM (e.g., Shakun and Carlson 2010; Shakun et al. 2012; Annan and Hargreaves 2015; Tierney et al. 2020). The patterns of hydrologic change are shown in Fig. 3b, which we computed using two approximations from Held and Soden (2006, hereafter HS06). First, if the atmospheric circulation stays about the same, F will roughly scale with atmospheric water vapor, which changes with T_s at the Clausius–Clapeyron rate of around 7% K^{-1} :

$$F' \approx 0.07FT_s'. \tag{20}$$

As long as T'_s is relatively uniform, the same scaling also applies to E - P (Fig. 3b, black line):

$$E' - P' \approx 0.07(E - P)T'_{s}$$
 (21)

Second, to separate E' - P' into its component parts, we assume that E scales with T_s at the global-mean rate of 2% K⁻¹ everywhere, thus essentially preserving its zonal-mean pattern (Fig. 3b, red line):

$$E' \approx 0.02ET_s'. \tag{22}$$

From Eqs. (21) and (22), the change in P (Fig. 3b, blue line) is then given by

$$P' \approx (0.07P - 0.05E)T'_{\rm s}.$$
 (23)

Despite their simplicity, the HS06 approximations have been shown to capture important aspects of the hydrologic response in GCM simulations of greenhouse warming, including the amplification of the mean-state E-P pattern (i.e., "wet gets wetter, dry gets drier") and the decrease in subtropical P (HS06), making them a useful benchmark against which more sophisticated approximations will later be compared.

Figure 3c shows the predicted change in $\overline{\delta_p}$ caused by the patterns of hydroclimate change in Figs. 3a and 3b. Comparing these changes with the mean-state pattern of $\overline{\delta_p}$ in Fig. 2c, we find that $\overline{\delta_p}$ generally decreases with cooling in the subtropics, where mean-state values are relatively high, and increases in the deep tropics and at high latitudes, where mean-state values are relatively low. In other words, cooling results in a flattening of the meridional $\overline{\delta_p}$ gradient.

To estimate the temporal slope $d\overline{\delta_p}/dT_s$, we divide the pattern of $\overline{\delta_p'}$ in Fig. 3c by the pattern of T_s' in Fig. 3a. The result, shown in Fig. 3d (black line), indicates positive slopes at low to middle latitudes and negative slopes poleward of $\sim 60^\circ$ in both hemispheres. We find a similar result if we assume that fractionation is fixed at 10% (Fig. 3d, gray line), implying that the temporal slope is mostly driven by changes in $\overline{\tau}$ resulting from E' and P', and not by the temperature dependence of

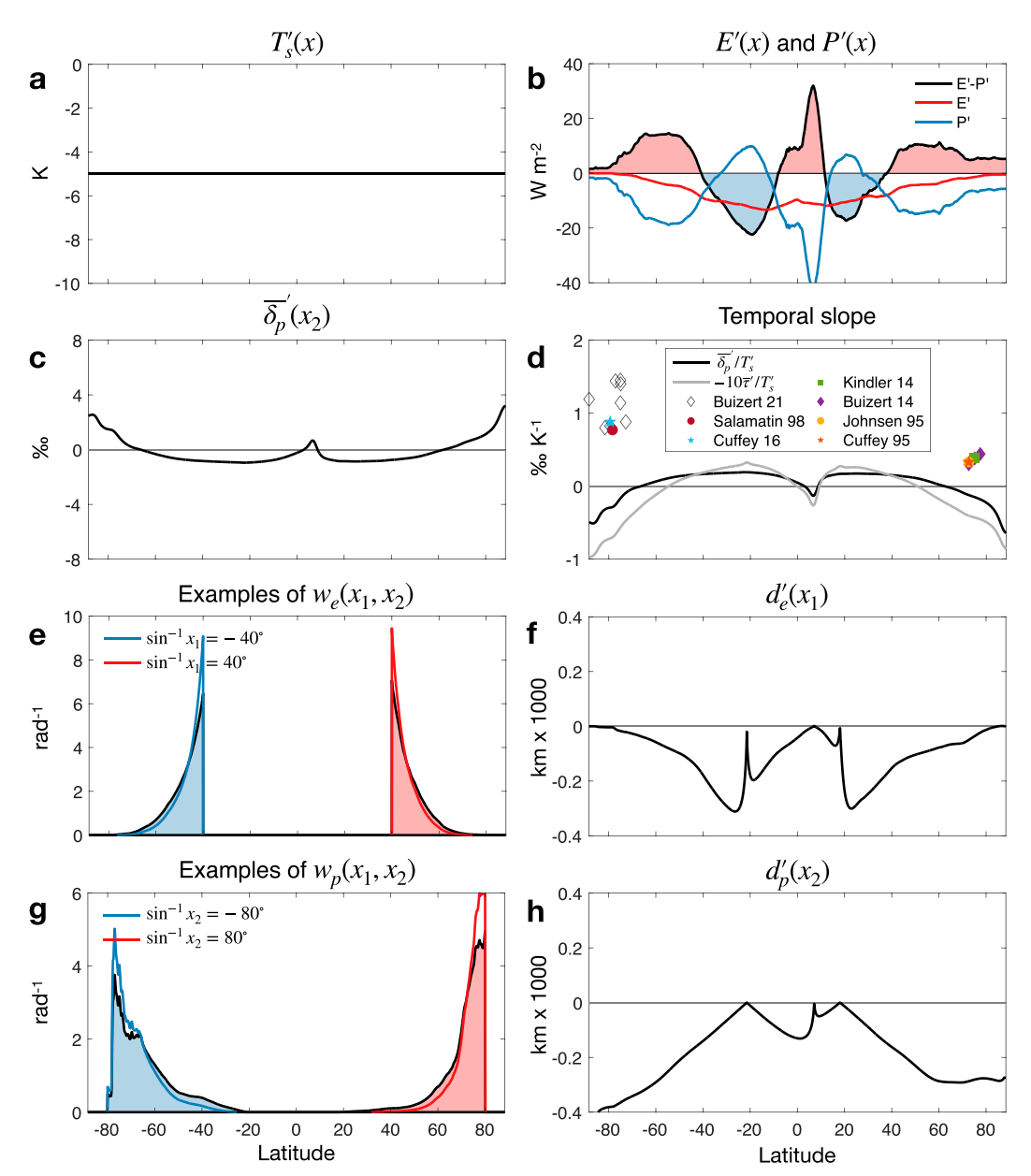


FIG. 3. Scenario 1: uniform global cooling. (a) Change in zonal-mean T_s . (b) Changes in zonal-mean E (red), P (blue), and E-P (black). (c) Change in $\overline{\delta_p}$. (d) The temporal slope (black line), approximated as the ratio of $\overline{\delta_p'}$ in (c) to T_s' in (a). The gray line shows the temporal slope assuming constant fractionation of 10% Colored symbols represent independent estimates of the temporal slope from polar ice cores (Table D1 and appendix D). (e) $w_e(x_1, x_2)$ at the same latitudes as in Fig. 1c. Shading represents the modern climate, while colored lines represent the cooler climate. (f) Change in the average distance vapor travels from each source latitude. (g) $w_p(x_1, x_2)$ at the same latitudes as in Fig. 1d. Shading represents the modern climate, while colored lines represent the cooler climate. (h) Change in the average distance vapor travels to each sink latitude.

fractionation. Significantly, the negative slopes at high latitudes contradict estimates of the temporal slope inferred from polar ice cores, which are all positive (Fig. 3d, symbols; see also Table D1 and appendix D).

To understand why cooling causes $\bar{\tau}$ to decrease (and $\bar{\delta_p}$ to increase) at high latitudes in this scenario, recall that the hydrologic attenuation coefficient μ is proportional to P/F [Eq.

(5)]. Under uniform global cooling, Eqs. (20) and (23) imply that P will decrease at a lower rate than F:

$$\frac{1}{P}\frac{dP}{dT_s} < \frac{1}{F}\frac{dF}{dT_s}.$$
 (24)

As a result, μ will generally increase with cooling. And because μ represents an inverse transport length scale, an increase in

 μ implies that water vapor will travel a shorter distance on average before condensing. This is confirmed in the third row of Fig. 3, which shows a more localized distribution of precipitation resulting from evaporation at 40° latitude (w_e ; Fig. 3e), and a global-scale decrease in the average distance that vapor travels after evaporating ($\overline{d_e}$; Fig. 3f). This result is consistent with GCM simulations, which show an increase in vapor transport distance in response to anthropogenic global warming (Singh et al. 2016b). It also suggests a decrease in atmospheric residence time, provided that changes in atmospheric dynamics are small by comparison (Trenberth 1998; Singh et al. 2016b).

An increase in μ with cooling has two competing effects on $\overline{\tau}$, which reflect opposing changes in τ and w_p [the two terms on the RHS of Eq. (19)]. On one hand, $\tau(x_1, x_2)$ increases, reflecting the fact that vapor on average travels a shorter distance before condensing. Therefore, if we only consider the component of local precipitation that evaporates at a single latitude, we would expect $\overline{\tau}$ to increase in a cooler climate (and $\overline{\delta_p}$ to decrease), consistent with the conventional Rayleigh understanding of the temperature effect (Dansgaard 1964).

On the other hand, μ also affects where vapor at a given latitude originates, as shown in the fourth row of Fig. 3. Given a uniform fractional change in E [as implied by Eq. (22) under uniform cooling], an increase in μ makes $w_p(x_1, x_2)$ more localized (Fig. 3g), implying that water vapor originates from closer by (Fig. 3h). And since heavy isotopes become more depleted the farther vapor travels along a given pathway, this contraction of $w_p(x_1, x_2)$ causes $\overline{\tau}$ to decrease in a cooler climate (and $\overline{\delta_p}$ to increase).

To understand which effect dominates and where, it is helpful to consider the limit of weak vapor transport, in which $F \to 0$ and $\mu \to \infty$. Applied to Eq. (19), this limit yields $\bar{\tau}=1$ everywhere (see appendix E). Under uniform global cooling, an increase in μ tends to nudge $\bar{\tau}$ toward this weak-transport limit. In other words, $\bar{\tau}$ tends to increase with cooling in the subtropics, where $\bar{\tau}(x) < 1$, and decrease with cooling in the deep tropics and at high latitudes, where $\bar{\tau}(x) > 1$. This results in a flattening of the meridional gradients in both $\bar{\tau}$ and δ_{p} , explaining the negative regression slope between δ_{p} and T_{s} at high latitudes. That this result contradicts observational estimates of the temporal slope from polar ice cores suggests that some important physics must be missing from our approximations of hydroclimate change in this scenario.

b. Scenario 2: Polar amplification

The analyses for the second scenario are presented in Fig. 4. We keep the HS06 approximation for evaporation sensitivity [Eq. (22)] but use a moist energy balance model (MEBM; Roe et al. 2015; Siler et al. 2018; Bonan et al. 2018; Armour et al. 2019) to calculate spatial patterns of T_s' and E' - P'. The MEBM assumes a downgradient transport of near-surface moist static energy and incorporates a Hadley cell parameterization that gives it a realistic hydrologic cycle (Siler et al. 2018). When forced with zonal-mean patterns of radiative forcing, feedbacks, and ocean heat uptake diagnosed from GCMs, the MEBM replicates most of the spatial structure of T_s'

and E' - P' simulated by the GCMs in response to increasing atmospheric CO₂ (Siler et al. 2018).

In this scenario, we impose a spatially uniform feedback of $\lambda = -1 \,\mathrm{W\,m^{-2}\,K^{-1}}$ and a spatially uniform radiative forcing of $-5 \,\mathrm{W\,m^{-2}}$. This produces the same magnitude of global-mean cooling that we prescribed in the HS06 analysis ($-5 \,\mathrm{K}$), but with significant polar amplification (Fig. 4a), reflecting a decrease in poleward latent heat transport as the meridional vapor gradient decreases under global cooling (Roe et al. 2015). As a result of polar amplification, the patterns of E' and P' also exhibit larger changes at high latitudes and smaller changes at low latitudes relative to the uniform-warming scenario (Fig. 4b).

By itself, however, polar amplification does not fundamentally change the spatial patterns of $\overline{\delta_p^\prime}$ or the temporal slope (Figs. 4c,d). From the source perspective, μ still increases nearly everywhere, reducing the average distance vapor travels after evaporating (Figs. 4e,f). Likewise, from the sink perspective, there is a broad decrease in the average distance that precipitation at a given latitude travels from its source (Figs. 4g,h). As in the uniform-warming scenario, these changes in vapor transport contribute to a flattening of the spatial patterns of $\overline{\delta_p}$ and $\overline{\tau}$ under cooling. This implies a negative temporal slope at high latitudes in contradiction to ice-core estimates (Figs. 4c,d), suggesting that an important piece of physics must still be missing.

c. Scenario 3: Temperature-dependent evaporation sensitivity

The analyses for the third scenario are presented in Fig. 5. In this scenario we again use the MEBM, but now also include a final piece of physics: a change in the spatial pattern of evaporation, as derived from the Penman equation (Penman 1948; Siler et al. 2019). Using this equation, Siler et al. (2019) showed that the zonal-mean change in evaporation in CMIP5 simulations of global warming is well approximated as

$$E' \approx -\frac{R_s' - G'}{1 + \beta_0} + \frac{ET_s'\beta_0(\tilde{\alpha} - 2/T_s)}{1 + \beta_0},$$
 (25)

where R'_s is the change in net downwelling radiation at the surface, G' is the change in ocean heat uptake/divergence,

$$\beta_0(T_s) = \frac{c_p}{\tilde{\alpha} L q * (T_s)} \tag{26}$$

is the Bowen ratio in the limit of a saturated near-surface atmosphere,

$$\tilde{\alpha}(T_s) = \frac{L}{R * T_s^2} \tag{27}$$

is the Clausius-Clapeyron scaling factor, q^* is the saturation specific humidity, and R^* is the specific gas constant of water vapor.

The first term on the RHS of Eq. (25) represents the contribution from the change in available energy at the surface $(R'_s - G')$. In radiative equilibrium, G' = 0 in the global mean, and can be neglected entirely if we assume a similar ocean circulation between the two climate states. Similarly, while R'_s

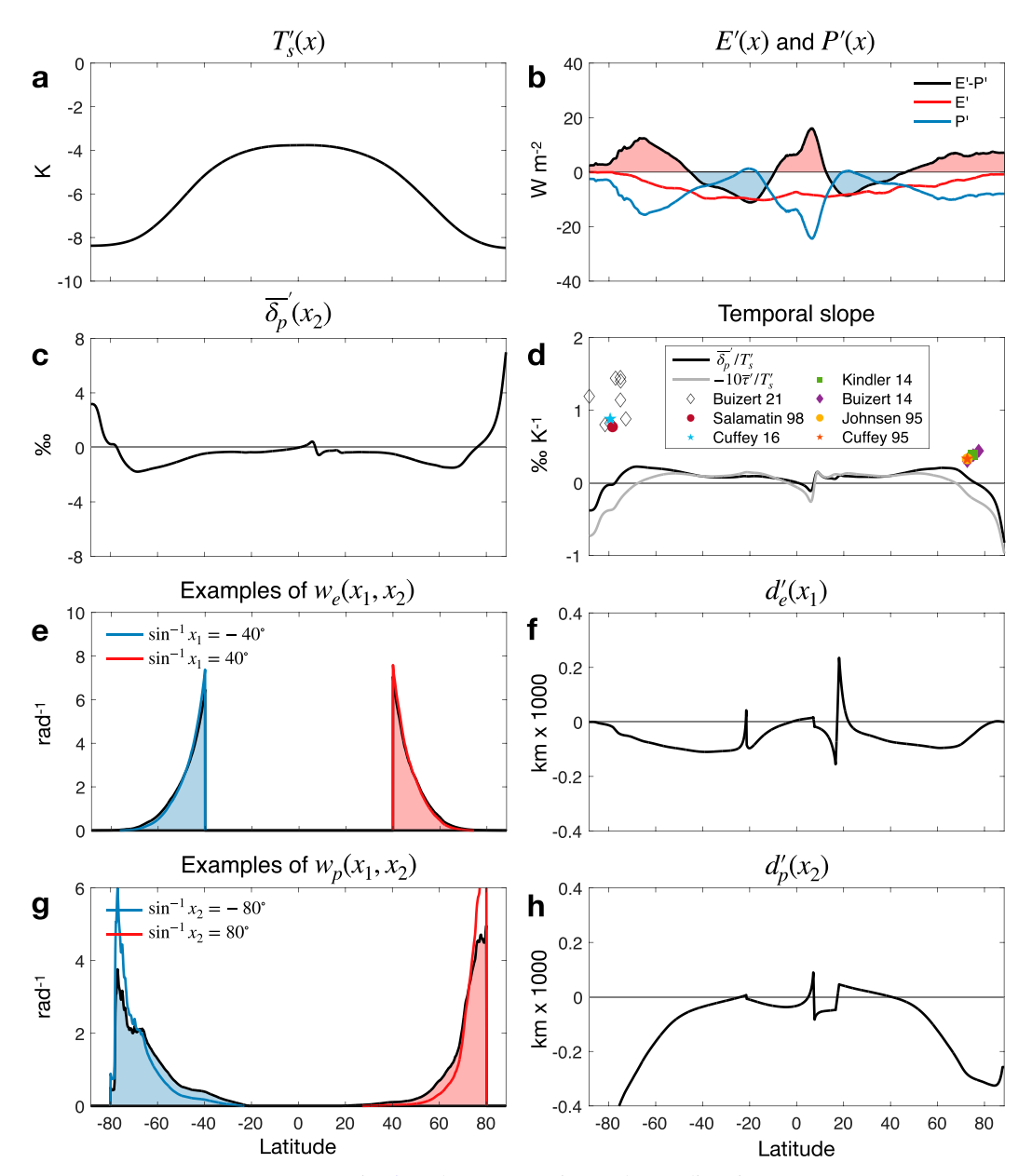


FIG. 4. As in Fig. 3, but for scenario 2: polar amplification.

is generally positive in GCM simulations of global warming, it has been shown to have minimal influence on the zonal-mean pattern of E' (Siler et al. 2018, 2019). For this reason, we follow Siler et al. (2018) and set $R'_s = 0$ as well.

That leaves the second term on the RHS of Eq. (25), which represents a thermodynamic constraint on the partitioning between latent and sensible heat fluxes. It corresponds to an evaporation sensitivity E'/ET'_s that decreases nearly linearly with T_s (supplemental Fig. 4), implying that evaporation is most sensitive to temperature change at high latitudes, where the mean-state temperature is coolest (Scheff and Frierson 2014; Siler et al. 2019). The result is a larger decrease in E at high latitudes and a smaller decrease at low latitudes compared

to the HS06 approximation (Fig. 5b vs Fig. 4b, red lines; see also Fig. 8 from Siler et al. 2018).

From the source perspective, the polar amplification of E' implied by Eq. (25) has only a modest effect on vapor transport distance. As in the previous two scenarios, $\overline{d_e}$ decreases nearly everywhere (Fig. 5f), indicating that vapor travels a shorter distance from its source under cooling.

From the sink perspective, however, the polar amplification of E' has a large impact (Figs. 5g,h). At high latitudes, in particular, the large decrease in E' locally means that precipitation comes from more remote regions on average, and thus travels a greater distance from its evaporation source, as indicated by an increase in $\overline{d_p}$ (Fig. 5h). Combined with the decrease in

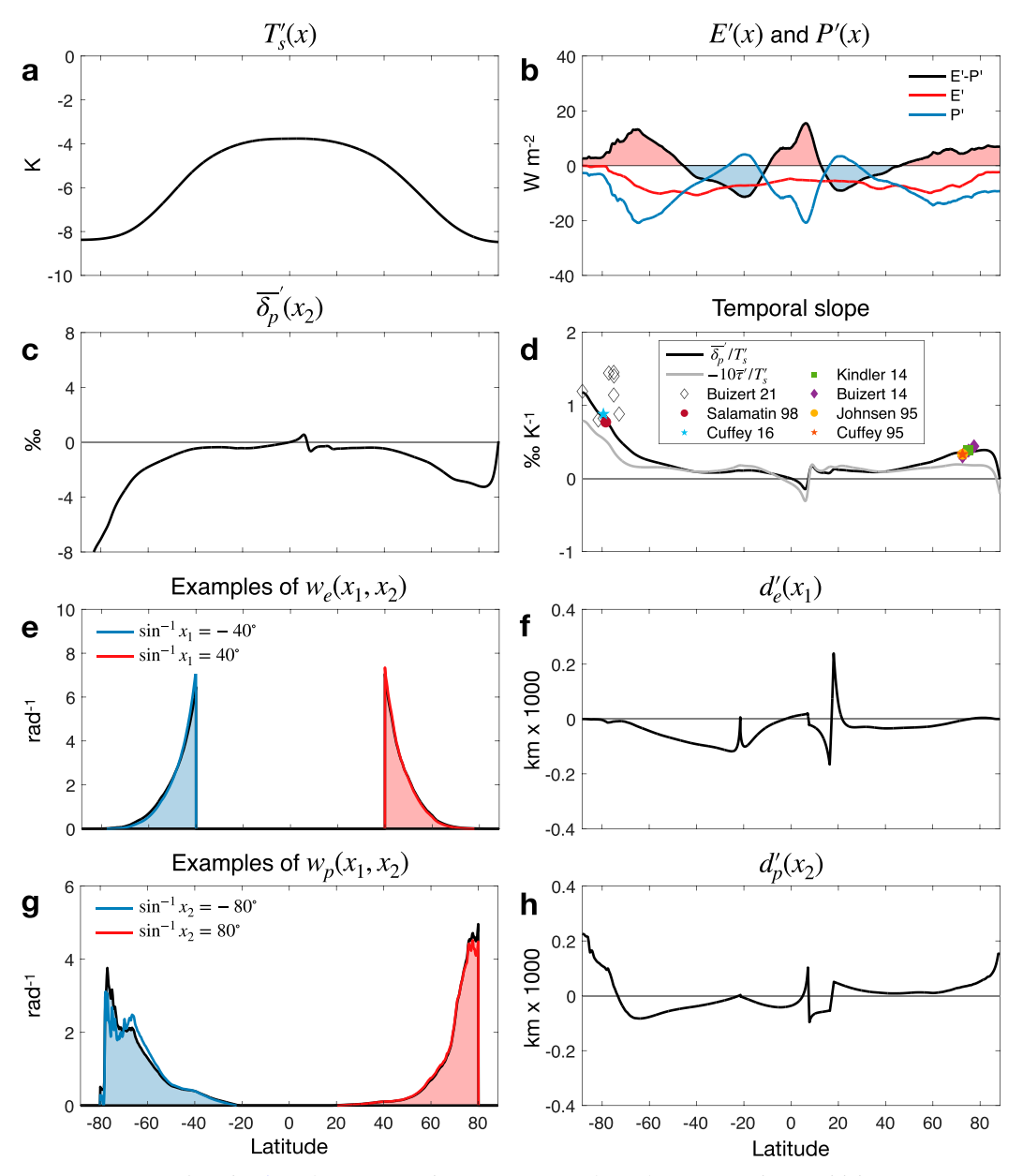


FIG. 5. As in Fig. 3, but for scenario 3: temperature-dependent evaporation sensitivity.

 $\delta_p(x_1, x_2)$ caused by greater attenuation, this increase in average transport distance results in a large decrease in $\overline{\delta_p}$ at high latitudes (Fig. 5c), in stark contrast to the previous two scenarios (Figs. 3c and 4c). The decrease in $\overline{\delta_p}$ implies a positive temporal slope that is within the range of ice-core estimates, albeit on the low end in Antarctica (Fig. 5d). Greater slopes over Antarctica might be achieved by accounting for the role of sea ice, whose expansion under cooling would likely result in a further suppression of high-latitude E and a greater depletion of high-latitude $\overline{\delta_p}$. In any case, the similarity between the gray and black lines in Fig. 5d confirms that the positive temporal slope is well represented by changes in the average path-integrated attenuation $\overline{\tau}$, implying that changes in the

temperature-dependent fractionation factor (α) play only a secondary role.

These results highlight an important distinction between the source and sink definitions of vapor transport distance. From the source perspective, transport distance is proportional to μ^{-1} , which decreases robustly with cooling. From the sink perspective, however, transport distance is set by the shape of w_p , which is quite sensitive to the spatial pattern of E [Eq. (8)]. Because E is most sensitive to temperature change at high latitudes, the distribution of vapor sources shifts equatorward under cooling. Thus, precipitation at high latitudes can originate from farther away under cooling, even as vapor on average travels a shorter distance from where it evaporates.

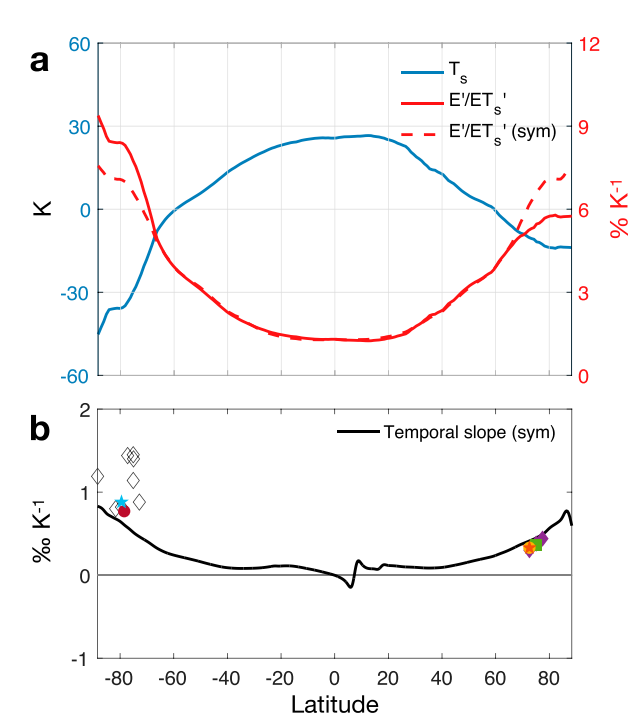


FIG. 6. (a) Zonal-mean T_s in the modern climate (blue) and the fractional change in zonal-mean E per degree of zonal-mean warming (red; E'/ET'_s) given by Eq. (25) with $G' = R'_s = 0$. The dashed red line shows a hemispherically symmetric pattern of E'/ET'_s , representing the average of the two hemispheres. (b) As in Fig. 5d, but with E' computed using the hemispherically symmetric scaling represented by the dashed line in (a).

5. Source of hemispheric asymmetry in the temporal slope

A striking aspect of the simulated temporal slope in Fig. 5d is that it captures much of the difference in observed temporal slopes between Antarctica, where the average exceeds 1% K $^{-1}$, and Greenland, where the average is less than 0.4% K $^{-1}$ (Table D1). Here we show that this asymmetry can be explained by hemispheric differences in the mean-state meridional temperature gradient.

Figure 6a shows the annual-mean, zonal-mean surface temperature in the modern climate (blue line), along with the local sensitivity of evaporation to temperature change (E'/ET'_s) given by Eq. (25) with $G' = R'_s = 0$ (solid red line). Poleward of about 65°, the Southern Hemisphere is significantly cooler than the Northern Hemisphere. While this asymmetry can be attributed in part to the Antarctic continent, similar differences exist over high-latitude oceans, where most evaporation occurs (supplemental Fig. 5). Because evaporation is most sensitive to temperature change at cool temperatures, this results in a larger meridional gradient in E'/ET'_s in the Southern Hemisphere than in the Northern Hemisphere. Therefore, given similar patterns of cooling in each hemisphere (Fig. 5a), the Southern Hemisphere will exhibit a larger equatorward shift in the spatial pattern of evaporation, contributing to larger shifts in the distribution of evaporation sources at high latitudes (Figs. 5g,h).

To test whether this effect can explain the hemispheric asymmetry in the temporal slope, we repeat our analysis of scenario 3, but adjust E' so that the pattern of E'/ET'_s is hemispherically symmetric (Fig. 6a, dashed red line). As expected, the resulting temporal slope (Fig. 6b) exhibits almost no difference between the Northern and Southern Hemispheres at high latitudes. This confirms that the hemispheric differences in the high-latitude temporal slope in scenario 3 (Fig. 5d) are indeed primarily the result of differences in the spatial pattern of evaporation change caused by differences in the mean-state meridional temperature gradient.

6. Sensitivity of the temporal slope to spatially varying feedbacks

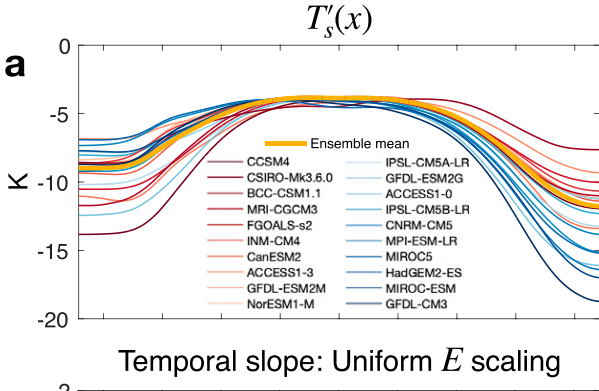
In section 4, our MEBM simulation of the LGM climate used in scenarios 2 and 3 assumed a spatially uniform radiative feedback of $-1 \text{ W m}^{-2} \text{ K}^{-1}$. In GCMs, however, feedbacks usually exhibit significant spatial variability, which can have a large impact on the patterns of E', P', and T'_e .

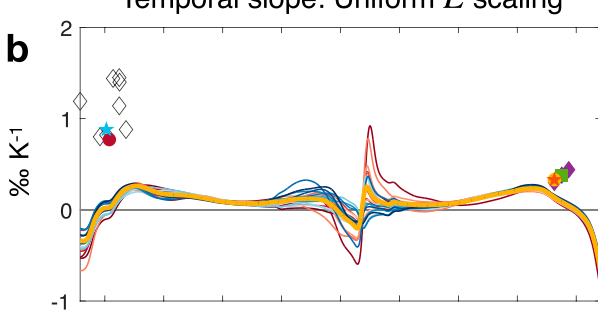
Here we test the sensitivity of the temporal slope to different feedback patterns by repeating our MEBM simulation of the LGM climate using the actual feedback patterns from 20 different GCMs, which we computed using the same method described in Siler et al. (2018). Because these feedback patterns are diagnosed from simulations of greenhouse warming, they likely misrepresent aspects of the radiative response to global cooling, particularly related to changes in ice albedo. Nevertheless, this approach provides a simple test of the robustness of our results given large model uncertainties in the spatial patterns of feedbacks and hydroclimate change.

Figure 7a shows the patterns of temperature change simulated by the MEBM given the same radiative forcing as before $(-5\,\mathrm{W\,m^{-2}})$, but with spatially varying feedbacks diagnosed from each GCM, which we have scaled to give a constant global-mean value of $-1\,\mathrm{W\,m^{-2}\,K^{-1}}$. The ensemble-mean response is shown in yellow, while the individual models are sorted according to the asymmetry of their temperature response, with deep blue indicating much more cooling in the Northern Hemisphere, and deep red indicating roughly equal cooling in both hemispheres.

Figure 7b shows the range of temporal slopes given by the different feedback patterns when we use the HS06 approximation for E', as in scenario 2. For all feedback patterns, the temporal slope is essentially unchanged from the uniform-feedback case (Fig. 4d). This shows that, given uniform evaporation scaling, varying patterns of feedbacks and temperature change are not sufficient to produce high-latitude temporal slopes that are consistent with the ice-core record.

In contrast, when we apply the Penman evaporation scaling from Eq. (25), we find that most feedback patterns yield temporal slopes that agree well with observations at high latitudes (Fig. 7c). Interestingly, the feedback patterns that give the worst agreement with observations are associated with much greater cooling in the Northern Hemisphere than in the Southern Hemisphere (deep blue lines). However, feedback-driven differences in the temporal slope are small compared





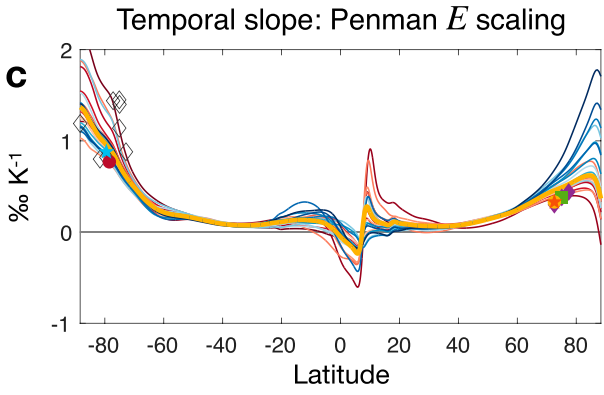


FIG. 7. (a) Change in zonal-mean T_s simulated by the MEBM with a uniform radiative forcing of $-5 \,\mathrm{W\,m^{-2}}$ and feedback patterns diagnosed from 20 CMIP5 models. The yellow line represents the ensemble mean. The other lines represent individual models, with deep blue indicating much more cooling in the Northern Hemisphere, and deep red indicating roughly equal cooling in both hemispheres. (b) The temporal slope $\delta_p^{\prime}/T_s^{\prime}$ computed using the HS06 approximation for E^{\prime} , as in scenario 2. (c) The temporal slope computed using the Penman approximation for E^{\prime} , as in scenario 3.

with those resulting from different representations of evaporation change (Fig. 7b vs Fig. 7c). This reinforces our conclusion from section 4c that the positive temporal slopes recorded in polar ice cores largely reflect shifts in the spatial pattern of evaporation with climate change.

7. Conclusions

In this paper, we have introduced a simple framework for quantifying the movement of water vapor and the spatial distribution of water isotopes within the zonal-mean climate. This framework is based on the fact that horizontal vapor transport within the atmosphere is attenuated by precipitation in much the same way that radiation is attenuated by scattering or absorption. In the zonal-mean hydrologic cycle, we find that the attenuation coefficient μ is proportional to P/|F|, or the ratio of precipitation to meridional vapor transport, and can therefore be determined from the zonal-mean patterns of P and evaporation E.

After finding μ , we use Beer's law to derive the hydrologic transmittance $f(x_1, x_2)$, which represents the fraction of water vapor that evaporates at a particular source latitude x_1 and reaches a particular sink latitude x_2 without precipitating. From f, we can estimate where vapor that evaporates at a particular latitude precipitates, and also where vapor that precipitates at a particular latitude evaporates. These distributions allow us to estimate the average meridional distance that vapor travels from a particular source latitude, as well as to a particular sink latitude. While the former is roughly proportional to μ^{-1} , the latter is strongly dependent on the spatial pattern of E.

Combining this radiative-transfer framework with a Rayleigh distillation model then allows us to solve for the zonal-mean δ of precipitation $\overline{\delta_p}$. We focus on $\delta^{18}O$ in this study, but our equations can easily be adapted for other meteoric isotopes like 2H (deuterium) or ^{17}O . We account for the influence of temperature and nonequilibrium kinetic effects on fractionation during both evaporation and condensation, but at least for $\delta^{18}O$, we find that these effects are much less important than attenuation, which is set by the zonal-mean patterns of E and E. This supports the idea that variations in E are largely driven by local and remote imbalances in E as several recent studies have suggested (e.g., Lee et al. 2008; Moore et al. 2014; Bailey et al. 2018).

Finally, we consider the factors that contribute to the observed temporal regression slope between $\overline{\delta_p}$ and temperature in polar ice cores. We simulate the response of $\overline{\delta_p}$ to three idealized patterns of hydroclimate change, all associated with a 5-K decrease in global-mean temperature representative of the Last Glacial Maximum. In each scenario, we find that μ increases with cooling because F decreases at a greater rate than P. If we assume that the spatial pattern of E stays about the same, an increase in μ results in a more uniform distribution of $\overline{\delta_p}$ across the globe. At high latitudes, this implies a negative temporal regression slope between $\overline{\delta_p}$ and temperature, which contradicts estimates derived from polar ice cores. That the temporal slope is in fact positive at high latitudes thus requires a shift in E toward the tropics under global cooling and toward the poles under global warming. We demonstrate that this shift can be explained by thermodynamic constraints on the partitioning between latent and sensible heat fluxes, as predicted by the Penman equation. However, we acknowledge that other factors may also play a role, including changes in ocean circulation, the latitude of the midlatitude storm tracks (e.g., Aemisegger and Papritz 2018; Aemisegger 2018), and especially sea ice extent (e.g., Noone and Simmonds 2004; Singh et al. 2017). Further research is needed to assess the relative importance of these factors.

Our analyses demonstrate that the δ^{18} O-temperature relationship at high latitudes reflects the coherent response of

temperature, heat transport, and hydrology over large spatial scales. While traditional explanations of the $\delta^{18}O$ –temperature relationship tend to focus on how temperature change alters the progressive fractionation of isotopes, our analyses show that the changing pattern of evaporation also plays an essential role.

This result points to a potential limitation of 18 O paleothermometry that we have not directly addressed here: namely, a decrease in δ^{18} O in ice cores need not necessarily be accompanied by global- or even local-scale cooling, but could in principle result from *any* event that disproportionately reduces high-latitude evaporation. For example, one could imagine past episodes of hemisphere- or basin-specific expansions in sea ice that were driven not by cooling, but by regional changes in ocean dynamics, salinity, or stratification (e.g., Bintanja et al. 2015; Pauling et al. 2016, 2017). Distinguishing the isotopic signatures of such processes from those of local and global temperature variability is an important avenue for future research.

Acknowledgments. We thank Stefan Terzer-Wassmuth for help accessing the IAEA/GNIP database. We thank Mathieu Casado and two anonymous reviewers for very helpful suggestions. NS was supported by NSF Grant AGS-1954663. CB was supported by NSF Grants ANT-1643394 and ARC-1804154. DN was supported by NSF Grant AGS-1502806. This material is based upon work supported by the National Center for Atmospheric Research, which is a major facility sponsored by the National Science Foundation under Cooperative Agreement 1852977.

Data availability statement. ERA5 monthly mean evaporation, precipitation, and 2-m air temperature over the period 1979–2018 are available at https://climate.copernicus.eu/climate-reanalysis. Temperature and energy fluxes from the fifth-generation Coupled Model Intercomparison Project (CMIP5) are available at https://esgf-node.llnl.gov/search/cmip5/. Observations of precipitation δ^{18} O are available at https://www.iaea.org/services/networks/gnip. Observational estimates of the temporal regression slope between δ^{18} O and temperature in polar ice cores were taken from publications cited in Table D1.

APPENDIX A

Approximation of $\overline{d_e}(x_1)$ in Eq. (10)

Over most of the globe, $\mu(x)$ varies much less over small scales than does $f(x_1, x_2)$, which exhibits exponential decay [Eq. (4)]. If we assume that μ is approximately constant over the length scale of $f(x_1, x_2)$, then we can approximate Eq. (7) as

$$w_{\rho}(x_1, x_2) \approx \mu(x_1)e^{-\tau(x_1, x_2)}$$
. (A1)

Similarly, the distance between source and sink latitudes is approximately

$$a|\theta_2 - \theta_1| \approx \frac{a|x_2 - x_1|}{\cos \theta_1},\tag{A2}$$

based on the relation $dx = d\theta \cos\theta$. For simplicity, let us assume that $x_2 > x_1$, meaning that vapor transport is northward at the source latitude. Substituting Eqs. (A1) and (A2) into Eq. (9) then gives

$$\overline{d_e}(x_1) \approx \frac{a\mu(x_1)}{\cos \theta_1} \int_{x_1}^1 (x_2 - x_1) e^{-\tau(x_1, x_2)} dx_2.$$
 (A3)

To evaluate this integral, we substitute $x_2 - x_1 \approx \mu(x_1)^{-1}$ $\tau(x_1, x_2)$ and $dx_2 \approx \mu(x_1)^{-1} d\tau$. These approximations derive from Eq. (2), based again on the assumption that $\mu(x_2) \approx \mu(x_1)$ over relevant transport scales. Because F = 0 at the poles, $\tau = \infty$ at $x_2 = 1$, while $\tau = 0$ at $x_2 = x_1$. Therefore, we integrate from $\tau = 0$ to ∞ :

$$\overline{d_e}(x_1) \approx \frac{a\mu(x_1)}{\cos\theta_1} \frac{1}{\mu(x_1)^2} \int_0^\infty \tau e^{-\tau} d\tau.$$
 (A4)

The integral in Eq. (A4) is equal to 1, yielding the approximation for $\overline{d_e}(x_1)$ in Eq. (10). The same result can be shown to apply for southward transport in which $x_2 < x_1$.

APPENDIX B

Temperature Dependence of α

When the effective fractionation factor for condensation (α) depends on the condensation temperature T_c , $R_p(x_1, x_2)$ is approximately equal to (Dansgaard 1964)

$$R_p(x_1, x_2) \approx \alpha(\overline{T_c}[x_2]) R_e(x_1) f(x_1, x_2)^{\overline{\alpha}(x_1, x_2) - 1}$$
 (B1)

Here α is the effective fractionation factor of condensation, which we parameterize as a function of the column-mean condensation temperature $\overline{T_c}(x_2)$, and $\overline{\alpha}(x_1, x_2)$ is the average effective fractionation factor over the lifetime of a vapor parcel that evaporates at x_1 and is transported to x_2 .

We approximate the column-mean condensation temperature as

$$\overline{T_c}(x) \approx \frac{\int_0^\infty T(x,z)C(x,z)\,dz}{\int_0^\infty C(x,z)\,dz},\tag{B2}$$

where T(x, z) is the average vertical temperature profile at x during condensation and C(x, z) is the condensation rate per distance of vertical displacement. To approximate these variables, we consider the idealized case of a saturated air parcel that ascends from the surface to the tropopause, which is a reasonable assumption during strong precipitating storms. In this scenario, equivalent potential temperature θ_e is conserved as a parcel ascends, implying that

$$C(x,z) = -\rho \frac{dq^*}{dz}\Big|_{\theta_e} \approx \rho \frac{dq^*}{dT} \Gamma_m, \tag{B3}$$

where ρ is the air density, q^* is the saturation specific humidity, (A2) and $\Gamma_m = -dT/dz|_{\theta_e}$ is the moist adiabatic lapse rate. For $q^*(T)$, we use an approximate form of the Clausius–Clapeyron equation,

$$q^*(T) \approx q^*(T_s)e^{\tilde{\alpha}\Delta T},$$
 (B4)

where $\Delta T = T - T_s$ and $\tilde{\alpha}(T_s)$ is the Clausius–Clapeyron scaling factor defined in Eq. (27). Differentiating Eq. (B4) gives $dq^*/dT = \tilde{\alpha}q^*$, which we combine with Eq. (B3) to get

$$C(x,z) \approx \rho \tilde{\alpha} q^* \Gamma_m.$$
 (B5)

We assume for simplicity that Γ_m is independent of z, implying that T decreases linearly with height:

$$T(x,z) \approx T_s(x) - \Gamma_m(x)z$$
. (B6)

From Eqs. (B4) and (B6), the vertical profile of water vapor is then given by

$$q^*(x,z) \approx q^*(x,0)e^{-\tilde{\alpha}\Gamma_m z}.$$
 (B7)

Finally, substituting Eqs. (B5)-(B7) into (B2) gives

$$\overline{T_s}(x) \approx T_s(x) - \tilde{\alpha}(T_s)^{-1}$$
. (B8)

We approximate $\alpha(\overline{T_c})$ in Eq. (B1) following previous models (e.g., Jouzel and Merlivat 1984; Petit et al. 1991; Ciais and Jouzel 1994; Hoffmann et al. 1998; Kavanaugh and Cuffey 2003). It is equal to the average of the fractionation factors for liquid and ice, weighted by the relative abundance of each species at a given condensation temperature:

$$\alpha(\overline{T_c}) = f_l(\overline{T_c})\alpha_l(\overline{T_c}) + [1 - f_l(\overline{T_c})]\alpha_i(\overline{T_c})\alpha_k(\overline{T_c}).$$
 (B9)

Here α_l and α_i are the temperature-dependent equilibrium fractionation factors for liquid-vapor and ice-vapor transitions, which we take from Majoube (1970, 1971); f_l is a weighting function representing the temperature-dependent fraction of total cloud water that is in the liquid phase, which Markle (2017) estimated from satellite observations; and α_k accounts for kinetic effects resulting from supersaturation at low temperatures.

To estimate α_k , we follow Jouzel and Merlivat (1984):

$$\alpha_k = \frac{S_i}{1 + \alpha_i \alpha_d (S_i - 1)},\tag{B10}$$

where $\alpha_d = 1.0285$ is the fractionation factor for molecular diffusion of snow and S_i is the supersaturation, which is parameterized as a linear function of $\overline{T_c}$ (in °C):

$$S_i = 1 - C\overline{T_c}. (B11)$$

Most previous studies have assumed values for C that range anywhere from 0.002 (e.g., Landais et al. 2008) to 0.008 (Schoenemann and Steig 2016). However, Markle (2017) has argued that values of C at the extremes of this range are inconsistent with the observed relationship between δ^{18} O and δ^2 H in global precipitation. Following Markle (2017), we choose a value near the middle of this range (C = 0.00525), but note that values of 0.007 and 0.003 give broadly similar results for the high-latitude temporal slope as those presented in section 4 (supplemental Fig. 6). This parameterization yields the profile of α (T_c) shown in purple

in supplemental Fig. 2. We then smooth this curve to account for the spread in condensation temperatures about $\overline{T_c}$ at a given latitude (black line).

To approximate $\overline{\alpha}(x_1, x_2)$ in Eq. (B1), we compute the average value of $\alpha(T_c)$ over the temperature range $T_s(x_1) < T_c < \overline{T_c}(x_2)$, weighted by the amount of condensation that occurs at each temperature (dq^*/dT_c) . Because q^* is approximately exponential, $dq^*/dT_c \propto q^*(T_c)$, and the weighted average simplifies to

$$\overline{\alpha}(x_1, x_2) \approx \frac{\int_{T_c(x_1)}^{\overline{T_c}(x_2)} \alpha(T_c) q^*(T_c) dT_c}{\int_{T_c(x_1)}^{\overline{T_c}(x_2)} q^*(T_c) dT_c}.$$
 (B12)

APPENDIX C

Implementation of the Craig-Gordon Model

The Craig-Gordon model (Craig and Gordon 1965) represents a simple parameterization of the influence of temperature and nonequilibrium kinetics on the isotope ratio of water vapor as it evaporates from the ocean surface. We implement it using the following equation (e.g., Hoffmann et al. 1998; Lee et al. 2008):

$$\delta_e = \frac{\delta_o - h\delta_v + 1000(\alpha_e^{-1} - 1)}{1 - h} + \Delta_k,$$
 (C1)

where $\alpha_e(T_s)$ is the equilibrium fractionation factor for conversion from liquid to vapor, h is the relative humidity with respect to sea surface temperature, Δ_k is an empirical correction that accounts for kinetic effects, and δ_e , δ_o , and δ_v represent the isotopic composition of the evaporative flux, ocean water, and near-surface atmosphere, respectively. Each δ_x can be converted to an isotope ratio R_x using Eq. (13). We set r=0.7, $\delta_o=0$, and $\Delta_k=-6$ (following Lee et al. 2008).

The remaining two variables, δ_e and δ_v , must be solved iteratively. Because δ_v depends on the fractionation of vapor that evaporates upstream, we compute it as the weighted average of upstream sources, analogous to $\overline{\delta_p}$ in Eq. (12). However, we recognize that the near-surface atmosphere is more likely than the rest of the atmospheric column to contain vapor that evaporates locally. To account for this, we replace $w_p(x_1, x_2)$ with a weighting function $w_v(x_1, x_2)$ that gives more weight to local sources:

$$w_{v}(x_{1}, x_{2}) = \frac{f(x_{1}, x_{2})^{\kappa} E(x_{1})}{\int_{-1}^{1} f(x_{1}, x_{2})^{\kappa} E(x_{1}) dx_{1}},$$
 (C2)

where κ is a free parameter. We have experimented with different values of κ ranging from 1 (which gives $w_v = w_p$) to 2. Comparing the resulting values of δ_v and δ_e in the modern climate with Fig. 11 from Lee et al. (2008), we find the best agreement by setting $\kappa = 1.5$ (supplemental Fig. 3). This value is therefore used for all simulations.

TABLE D1. Estimates of the temporal regression slope between the $\delta^{18}O$ of snow and local surface temperature $(d\delta_p/dT_s)$ based on analyses of ice cores in Greenland and Antarctica spanning the LGM-Holocene deglaciation. The first column gives the temporal slope (in % K⁻¹), followed by the name and coordinates of the ice core, the analysis method, and the source. Further details are given in appendix D.

$d\delta_p/dT_s$	Site	Longitude (°)	Latitude (°)	Method	Source
Greenland					
0.33	GISP2	-38.48	72.58	Borehole	Cuffey et al. (1995)
0.30	GISP2	-38.48	72.58	δ^{15} N	Buizert et al. (2014)
0.33	GRIP	-37.64	72.58	Borehole	Johnsen et al. (1995)
0.38	NGRIP	-42.32	75.10	$\delta^{15} N$	Kindler et al. (2014)
0.38	NGRIP	-42.32	75.10	$\delta^{15} N$	Buizert et al. (2014)
0.44	NEEM	-51.06	77.45	$\delta^{15} N$	Buizert et al. (2014)
Antarctica					
0.88	Talos Dome	159.18	-72.82	Firn reconstruction	Buizert et al. (2021)
1.40	EDML	0	-75	Firn reconstruction	Buizert et al. (2021)
1.14	Dome C	123.3	-75.1	Borehole	Buizert et al. (2021)
1.45	EDC	123.3	-75.1	Firn reconstruction	Buizert et al. (2021)
1.44	Dome F	39.42	-77.19	Firn reconstruction	Buizert et al. (2021)
0.77	Vostok	106.80	-78.47	Borehole	Salamatin et al. (1998)
0.88	WAIS Divide	-112.10	-79.48	Borehole	Cuffey et al. (2016)
0.82	WAIS Divide	-112.10	-79.48	Firn reconstruction	Buizert et al. (2021)
0.80	Siple Dome	-148.81	-81.65	Firn reconstruction	Buizert et al. (2021)
1.19	South Pole	0	-90	Firn reconstruction	Buizert et al. (2021)

APPENDIX D

Observational Estimates of the Temporal Slope from Polar Ice Cores

The symbols shown in Figs. 3d, 4d, and 5d and in Figs. 6b, 7b, and 7c represent estimates of the temporal slope derived from analyses of water isotope variability in polar ice cores, as summarized in Table D1. Because our analysis focuses on differences between the LGM and the modern climate, we only consider slope estimates that are derived from direct analysis of ice-core variability over the last deglaciation (i.e., from the LGM to the Holocene). We do not consider estimates that are based on GCM simulations, spatial regression slopes, or ice-core analyses that do not span the last deglaciation.

All values of the temporal slope in Table D1 are taken directly from the published sources, with a few caveats. First, in cases where only a δ^2 H slope was published, we have divided that value by 8 to make it comparable to the δ^{18} O slope. Second, the slope of 0.33‰ K⁻¹ for the GRIP core that we attribute to Johnsen et al. (1995) is derived from their Eq. (1), using their parameters and their values of $dT_s/d\delta_p$ from the LGM and Holocene. Third, the slope of 0.38‰ K⁻¹ for the NGRIP core that we attribute to Kindler et al. (2014) is derived from their Fig. 3a, which shows an increase in δ^{18} O of about 6‰ along with an increase in temperature of about 16 K between the LGM and the beginning of the Holocene.

APPENDIX E

Evaluating $\overline{\tau}$ in the Weak-Transport Limit

To find $\bar{\tau}$ in the limit of weak vapor transport $(F \to 0)$, we begin with Eq. (19) and use the relation $d\tau/dx = \mu$ to change

the variable of integration from dx_1 to $d\tau/\mu$. Because vapor only travels to x_2 from the upstream direction (determined by the sign of F), and because $\tau = \infty$ at the poles (see appendix A above), we can write Eq. (19) as

$$\bar{\tau} = \frac{\int_{0}^{\infty} \tau \mu^{-1} E e^{-\tau} d\tau}{\int_{0}^{\infty} \mu^{-1} E e^{-\tau} d\tau}.$$
 (E1)

Here $\tau = 0$ at $x_1 = x_2$ (i.e., where the sink latitude equals the source latitude) and increases to infinity as x_1 moves farther upstream.

As F decreases, μ increases, for reasons discussed in section 4a. Therefore, the transmittance $(f = e^{-\tau})$ decays more sharply (in physical space) away from the source latitude, reflecting a decrease in transport length scale. By contrast, there is no mechanism that would cause the scale of spatial variability in E or μ to decrease by a similar magnitude. Thus, as $F \to 0$, E and μ become essentially constant over the transport length scale, and can therefore be brought outside the integrals, where they cancel. Thus, in the weak-transport limit, Eq. (19) reduces to

$$\overline{\tau} \approx \frac{\int_{0}^{\infty} \tau e^{-\tau} d\tau}{\int_{0}^{\infty} e^{-\tau} d\tau} = 1.$$
 (E2)

Physically, this result is a necessary consequence of mass conservation. In the absence of horizontal transport, δ_p must equal δ_e everywhere. Under constant fractionation, both will be equal to $-\varepsilon$, and thus $\bar{\tau}$ must equal 1 [Eq. (17)].

REFERENCES

- Aemisegger, F., 2018: On the link between the North Atlantic storm track and precipitation deuterium excess in Reykjavik. *Atmos. Sci. Lett.*, **19**, e865, https://doi.org/10.1002/asl.865.
- —, and L. Papritz, 2018: A climatology of strong large-scale ocean evaporation events. Part I: Identification, global distribution, and associated climate conditions. *J. Climate*, 31, 7287– 7312, https://doi.org/10.1175/JCLI-D-17-0591.1.
- Allen, M., and W. J. Ingram, 2002: Constraints on future changes in climate and the hydrologic cycle. *Nature*, 419, 228–232, https:// doi.org/10.1038/nature01092.
- Annan, J., and J. Hargreaves, 2015: A perspective on model-data surface temperature comparison at the Last Glacial Maximum. *Quat. Sci. Rev.*, 107, 1–10, https://doi.org/10.1016/j.quascirev.2014.09.019.
- Armour, K. C., N. Siler, A. Donohoe, and G. H. Roe, 2019: Meridional atmospheric heat transport constrained by energetics and mediated by large-scale diffusion. *J. Climate*, 32, 3655–3680, https://doi.org/10.1175/JCLI-D-18-0563.1.
- Bailey, A., E. Posmentier, and X. Feng, 2018: Patterns of evaporation and precipitation drive global isotopic changes in atmospheric moisture. *Geophys. Res. Lett.*, 45, 7093–7101, https://doi.org/10.1029/2018GL078254.
- Bintanja, R., G. J. Van Oldenborgh, and C. A. Katsman, 2015: The effect of increased fresh water from Antarctic ice shelves on future trends in Antarctic sea ice. *Ann. Glaciol.*, **56**, 120–126, https://doi.org/10.3189/2015AoG69A001.
- Boer, G., 1993: Climate change and the regulation of the surface moisture and energy budgets. *Climate Dyn.*, 8, 225–239, https://doi.org/10.1007/BF00198617.
- Bonan, D. B., K. C. Armour, G. H. Roe, N. Siler, and N. Feldl, 2018: Sources of uncertainty in the meridional pattern of climate change. *Geophys. Res. Lett.*, 45, 9131–9140, https:// doi.org/10.1029/2018GL079429.
- Boyle, E. A., 1997: Cool tropical temperatures shift the global $\delta^{18}\text{O-}T$ relationship: An explanation for the ice core $\delta^{18}\text{O-}$ borehole thermometry conflict? *Geophys. Res. Lett.*, **24**, 273–276, https://doi.org/10.1029/97GL00081.
- Buizert, C., and Coauthors, 2014: Greenland temperature response to climate forcing during the last deglaciation. *Science*, **345**, 1177–1180, https://doi.org/10.1126/science.1254961.
- —, and Coauthors, 2021: Antarctic surface temperature and elevation during the Last Glacial Maximum. *Science*, 372, 1097–1101, https://doi.org/10.1126/science.abd2897.
- Charles, C. D., D. Rind, J. Jouzel, R. D. Koster, and R. G. Fairbanks, 1994: Glacial-interglacial changes in moisture sources for Greenland: Influences on the ice core record of climate. *Science*, 263, 508–511, https://doi.org/10.1126/science.263.5146.508.
- Ciais, P., and J. Jouzel, 1994: Deuterium and oxygen 18 in precipitation: Isotopic model, including mixed cloud processes. J. Geophys. Res., 99, 16 793, https://doi.org/10.1029/ 94JD00412.
- Craig, H., and L. Gordon, 1965: Deuterium and oxygen 18 variations in the ocean and the marine atmosphere. Stable Isotopes in Oceanographic Studies and Paleotemperatures, E. Tongiorgi, Ed., Università di Pisa Laboratorio di geologia nucleare, 9–130.
- Cuffey, K. M., R. B. Alley, P. M. Grootes, J. M. Bolzan, and S. Anandakrishnan, 1994: Calibration of the δ^{18} O isotopic paleothermometer for central Greenland, using borehole

- temperatures. *J. Glaciol.*, **40**, 341–349, https://doi.org/10.1017/S002214300007425.
- —, G. D. Clow, R. B. Alley, M. Stuiver, E. D. Waddington, and R. W. Saltus, 1995: Large Arctic temperature change at the Wisconsin-Holocene glacial transition. *Science*, 270, 455–458, https://doi.org/10.1126/science.270.5235.455.
- —, and Coauthors, 2016: Deglacial temperature history of West Antarctica. *Proc. Natl. Acad. Sci. USA*, **113**, 14 249–14 254, https://doi.org/10.1073/pnas.1609132113.
- Dahl-Jensen, D., K. Mosegaard, N. Gundestrup, G. D. Clow, S. J. Johnsen, A. W. Hansen, and N. Balling, 1998: Past temperatures directly from the Greenland Ice Sheet. *Science*, 282, 268–271, https://doi.org/10.1126/science.282.5387.268.
- Dansgaard, W., 1964: Stable isotopes in precipitation. *Tellus*, **16**, 436–468, https://doi.org/10.3402/tellusa.v16i4.8993.
- Fisher, D. A., 1990: A zonally-averaged stable-isotope model coupled to a regional variable-elevation stable-isotope model. *Ann. Glaciol.*, **14**, 65–71, https://doi.org/10.3189/S0260305500008284.
- Galewsky, J., H. C. Steen-Larsen, R. D. Field, J. Worden, C. Risi, and M. Schneider, 2016: Stable isotopes in atmospheric water vapor and applications to the hydrologic cycle. *Rev. Geophys.*, 54, 809–865, https://doi.org/10.1002/2015RG000512.
- Grootes, P. M., M. Stuiver, J. W. C. White, S. Johnsen, and J. Jouzel, 1993: Comparison of oxygen isotope records from the GISP2 and GRIP Greenland ice cores. *Nature*, 366, 552– 554, https://doi.org/10.1038/366552a0.
- Held, I. M., and B. J. Soden, 2006: Robust responses of the hydrological cycle to global warming. J. Climate, 19, 5686–5699, https://doi.org/10.1175/JCLI3990.1.
- Hersbach, H., and Coauthors, 2020: The ERA5 global reanalysis. *Quart. J. Roy. Meteor. Soc.*, **146**, 1999–2049, https://doi.org/10.1002/qj.3803.
- Hoffmann, G., M. Werner, and M. Heimann, 1998: Water isotope module of the ECHAM atmospheric general circulation model:
 A study on timescales from days to several years. *J. Geophys. Res.*, 103, 16 871–16 896, https://doi.org/10.1029/98JD00423.
- Johnsen, S. J., W. Dansgaard, and J. W. C. White, 1989: The origin of Arctic precipitation under present and glacial conditions. *Tellus*, 41B, 452–468, https://doi.org/10.1111/j.1600-0889.1989.tb00321.x.
- —, D. Dahl-Jensen, W. Dansgaard, and N. Gundestrup, 1995: Greenland palaeotemperatures derived from GRIP bore hole temperature and ice core isotope profiles. *Tellus*, **47B**, 624–629, https://doi.org/10.3402/tellusb.v47i5.16077.
- —, and Coauthors, 2001: Oxygen isotope and palaeotemperature records from six Greenland ice-core stations: Camp Century, Dye-3, GRIP, GISP2, Renland and NorthGRIP. *J. Quat. Sci.*, **16**, 299–307, https://doi.org/10.1002/jqs.622.
- Jouzel, J., and L. Merlivat, 1984: Deuterium and oxygen 18 in precipitation: Modeling of the isotopic effects during snow formation. J. Geophys. Res., 89, 11749, https://doi.org/10.1029/ JD089iD07p11749.
- —, and Coauthors, 1997: Validity of the temperature reconstruction from water isotopes in ice cores. *J. Geophys. Res. Oceans*, 102, 26 471–26 487, https://doi.org/10.1029/97JC01283.
- —, F. Vimeux, N. Caillon, G. Delaygue, G. Hoffmann, V. Masson-Delmotte, and F. Parrenin, 2003: Magnitude of isotope/temperature scaling for interpretation of central Antarctic ice cores. J. Geophys. Res., 108, 4361, https:// doi.org/10.1029/2002JD002677.
- Kavanaugh, J. L., and K. M. Cuffey, 2003: Space and time variation of δ^{18} O and δ D in Antarctic precipitation revisited.

- Global Biogeochem. Cycles, 17, 1017, https://doi.org/10.1029/2002GB001910.
- Kindler, P., M. Guillevic, M. Baumgartner, J. Schwander, A. Landais, and M. Leuenberger, 2014: Temperature reconstruction from 10 to 120 kyr b2k from the NGRIP ice core. *Climate Past*, 10, 887–902, https://doi.org/10.5194/cp-10-887-2014.
- Krinner, G., C. Genthon, and J. Jouzel, 1997: GCM analysis of local influences on ice core δ signals. *Geophys. Res. Lett.*, **24**, 2825–2828, https://doi.org/10.1029/97GL52891.
- Landais, A., E. Barkan, and B. Luz, 2008: Record of δ^{18} O and 17 O-excess in ice from Vostok Antarctica during the last 150,000 years. *Geophys. Res. Lett.*, **35**, L02709, https://doi.org/10.1029/2007GL032096.
- Lee, J.-E., I. Fung, D. J. DePaolo, and B. Otto-Bliesner, 2008: Water isotopes during the Last Glacial Maximum: New general circulation model calculations. *J. Geophys. Res. Atmos.*, 113, D19109, https://doi.org/10.1029/2008JD009859.
- Majoube, M., 1970: Fractionation factor of ¹⁸O between water vapour and ice. *Nature*, 226, 1242, https://doi.org/10.1038/2261242a0.
- —, 1971: Fractionnement en oxygène 18 et en deutérium entre l'eau et sa vapeur. J. Chim. Phys., 68, 1423–1436, https:// doi.org/10.1051/jcp/1971681423.
- Markle, B. R., 2017: Climate dynamics revealed in ice cores: Advances in techniques, theory, and interpretation. Ph.D. thesis, University of Washington, 214 pp.
- Masson-Delmotte, V., 2005: GRIP deuterium excess reveals rapid and orbital-scale changes in Greenland moisture origin. *Science*, 309, 118–121, https://doi.org/10.1126/science.1108575.
- —, and Coauthors, 2006: Past temperature reconstructions from deep ice cores: Relevance for future climate change. *Climate Past*, **2**, 145–165, https://doi.org/10.5194/cp-2-145-2006.
- Moore, M., Z. Kuang, and P. N. Blossey, 2014: A moisture budget perspective of the amount effect. *Geophys. Res. Lett.*, **41**, 1329–1335, https://doi.org/10.1002/2013GL058302.
- Noone, D., and I. Simmonds, 2004: Sea ice control of water isotope transport to Antarctica and implications for ice core interpretation. J. Geophys. Res. Atmos., 109, D07105, https://doi.org/ 10.1029/2003JD004228.
- Pauling, A. G., C. M. Bitz, I. J. Smith, and P. J. Langhorne, 2016: The response of the Southern Ocean and Antarctic sea ice to freshwater from ice shelves in an Earth system model. *J. Climate*, 29, 1655–1672, https://doi.org/10.1175/JCLI-D-15-0501.1.
- —, I. J. Smith, P. J. Langhorne, and C. M. Bitz, 2017: Time-dependent freshwater input from ice shelves: Impacts on Antarctic sea ice and the Southern Ocean in an Earth system model. *Geophys. Res. Lett.*, 44, 10 454–10 461, https://doi.org/10.1002/2017GL075017.
- Penman, H. L., 1948: Natural evaporation from open water, bare soil and grass. *Proc. Royal Soc. London*, **193A**, 120–145, https://doi.org/10.1098/rspa.1948.0037.
- Petit, J. R., J. W. White, N. W. Young, J. Jouzel, and Y. S. Korotkevich, 1991: Deuterium excess in recent Antarctic snow. J. Geophys. Res., 96, 5113–5122, https://doi.org/10.1029/90JD02232.
- Rhines, A., and P. J. Huybers, 2014: Sea ice and dynamical controls on preindustrial and last glacial maximum accumulation in central Greenland. J. Climate, 27, 8902–8917, https://doi.org/ 10.1175/JCLI-D-14-00075.1.
- Roe, G. H., N. Feldl, K. C. Armour, Y.-T. Hwang, and D. M. W. Frierson, 2015: The remote impacts of climate feedbacks on

- regional climate predictability. *Nat. Geosci.*, **8**, 135–139, https://doi.org/10.1038/ngeo2346.
- Salamatin, A. N., V. Y. Lipenkov, N. I. Barkov, J. Jouzel, J. R. Petit, and D. Raynaud, 1998: Ice core age dating and paleothermometer calibration based on isotope and temperature profiles from deep boreholes at Vostok Station (East Antarctica). J. Geophys. Res., 103, 8963–8977, https://doi.org/10.1029/97JD02253.
- Scheff, J., and D. M. W. Frierson, 2014: Scaling potential evapotranspiration with greenhouse warming. *J. Climate*, 27, 1539–1558, https://doi.org/10.1175/JCLI-D-13-00233.1.
- Schoenemann, S. W., and E. J. Steig, 2016: Seasonal and spatial variations of ¹⁷O_{excess} and d_{excess} in Antarctic precipitation: Insights from an intermediate complexity isotope model. *J. Geophys. Res.*, **121**, 11 215–11 247, https://doi.org/10.1002/2016JD025117.
- Severinghaus, J. P., T. Sowers, E. J. Brook, R. B. Alley, and M. L. Bender, 1998: Timing of abrupt climate change at the end of the Younger Dryas interval from thermally fractionated gases in polar ice. *Nature*, 391, 141–146, https://doi.org/10.1038/34346.
- Shakun, J. D., and A. E. Carlson, 2010: A global perspective on Last Glacial Maximum to Holocene climate change. *Quat. Sci. Rev.*, **29**, 1801–1816, https://doi.org/10.1016/j.quascirev.2010.03.016.
- —, and Coauthors, 2012: Global warming preceded by increasing carbon dioxide concentrations during the last deglaciation. *Nature*, 484, 49-54, https://doi.org/10.1038/nature10915.
- Siler, N., G. H. Roe, and K. C. Armour, 2018: Insights into the zonal-mean response of the hydrologic cycle to global warming from a diffusive energy balance model. *J. Climate*, 31, 7481–7493, https://doi.org/10.1175/JCLI-D-18-0081.1.
- —, —, and N. Feldl, 2019: Revisiting the surface-energy-flux perspective on the sensitivity of global precipitation to climate change. *Climate Dyn.*, **52**, 3983–3995, https://doi.org/10.1007/s00382-018-4359-0.
- Singh, H. K. A., C. M. Bitz, J. Nusbaumer, and D. C. Noone, 2016a: A mathematical framework for analysis of water tracers: Part 1: Development of theory and application to the preindustrial mean state. J. Adv. Model. Earth Syst., 8, 991–1013, https:// doi.org/10.1002/2016MS000649.
- —, —, A. Donohoe, J. Nusbaumer, and D. C. Noone, 2016b: A mathematical framework for analysis of water tracers. Part II: Understanding large-scale perturbations in the hydrological cycle due to CO₂ doubling. *J. Climate*, **29**, 6765–6782, https://doi.org/10.1175/JCLI-D-16-0293.1.
- —, —, and P. J. Rasch, 2017: A source-receptor perspective on the polar hydrologic cycle: Sources, seasonality, and Arctic–Antarctic parity in the hydrologic cycle response to CO₂ doubling. *J. Climate*, **30**, 9999–10017, https://doi.org/10.1175/JCLI-D-16-0917.1.
- Sodemann, H., and A. Stohl, 2009: Asymmetries in the moisture origin of Antarctic precipitation. *Geophys. Res. Lett.*, 36, L22803, https://doi.org/10.1029/2009GL040242.
- —, C. Schwierz, and H. Wernli, 2008: Interannual variability of Greenland winter precipitation sources: Lagrangian moisture diagnostic and North Atlantic Oscillation influence. J. Geophys. Res. Atmos., 113, D03107, https://doi.org/10.1029/2007JD008503.
- Tierney, J. E., J. Zhu, J. King, S. B. Malevich, G. J. Hakim, and C. J. Poulsen, 2020: Glacial cooling and climate sensitivity revisited. *Nature*, 584, 569–573, https://doi.org/10.1038/s41586-020-2617-x.

- Trenberth, K. E., 1998: Atmospheric moisture residence times and cycling: Implications for rainfall rates and climate change. *Climatic Change*, **39**, 667–694, https://doi.org/10.1023/A:1005319109110.
- Urey, H. C., 1947: The thermodynamic properties of isotopic substances. *J. Chem. Soc.*, **0**, 562–581, https://doi.org/10.1039/jr9470000562.
- Wallace, J. M., and P. V. Hobbs, 2006: Atmospheric Science: An Introductory Survey. Academic Press, 483 pp.
- Werner, M., U. Mikolajewicz, M. Heimann, and G. Hoffmann, 2000: Borehole versus isotope temperatures on Greenland: Seasonality does matter. *Geophys. Res. Lett.*, **27**, 723–726, https://doi.org/10.1029/1999GL006075.
- —, M. Heimann, and G. Hoffman, 2001: Isotopic composition and origin of polar precipitation in present and glacial climate simulations. *Tellus*, **53B**, 53–71, https://doi.org/10.3402/ tellusb.v53i1.16539.